JPE Journal of Photonics for Energy

RESEARCH PAPER

Hemispherical-shell-shaped organic photovoltaic cells for absorption enhancement and improved angular coverage

Dooyoung Hah*

Abdullah Gül University, Department of Electrical and Electronics Engineering, Faculty of Engineering, Kayseri, Türkiye

ABSTRACT. A hemispherical shell shape is proposed for an organic photovoltaic cell structure, aiming at enhancing both light absorption and angular coverage. Three-dimensional finite element analysis method is used to study the absorption spectra within the hemispherical-shell-shaped active layer. The study reveals that the proposed structure can result in 66% and 36% of absorption improvements compared to a flat-structured device when the incoming light is transverse electric (TE)- and transverse magnetic (TM)-polarized, respectively. It is also learned that the proposed hemispherical shell structure has absorption improvement as high as 13% (TE) and 21% (TM) when compared to the previously reported semicylindrical shell structure. The angular coverage of the proposed structure is improved as well, reaching 81 deg (TE) and 82 deg (TM), which becomes quite useful for the wearable electronics applications where the incidence angle can vary in a random manner. These improvements can be attributed to better light coupling and guiding through the active layer made possible by the hemispherical shell shape of the device.

 [DOI: 10.1117/1.JPE.14.018501]

Keywords: organic photovoltaic cells; light trapping; energy conversion efficiency; omnidirectionality

Paper 23045G received Oct. 23, 2023; revised Jan. 16, 2024; accepted Jan. 30, 2024; published Feb. 14, 2024.

1 Introduction

Energy is a major keyword at the present time as we are going through a series of global crises. Technology advancement in renewable energy has become quite imperative for humankind, and development in any aspect can lend a helping hand. In the field of solar energy technologies, significant progress has been made at various levels including materials, devices, circuits, storage, and systems, all of which have paramount impacts to the problems at hand. In this context, the current study focuses on performance improvement in solar cells at the device level from the optical design perspective.

A range of efforts have been made to enhance energy conversion efficiency in solar cells. Improving light coupling to and light retention in active photovoltaic layers has been one of the main research directions. These light management approaches are especially crucial in organic photovoltaic solar cells, which have a well-known length dilemma issue, i.e., the conflict between efficient photon absorption and charge carrier collection. Another performance indicator of organic photovoltaic cells is an angular coverage, which is especially important for wearable

*Address all correspondence to Dooyoung Hah, dooyoung.hah@agu.edu.tr

1947-7988/2024/$28.00 © 2024 SPIE

electronic system applications. Due to wide and random variations in light incidence angles in wearable applications, omnidirectionality is demanded from the solar cell devices.

A number of different approaches have been explored so far to improve light coupling/retention and angular coverage in solar cells. Several review articles are available on this topic.[1–7] Those attempts include surface nano-texturing,[8,9] embedded light scatterers,[10–12] excitation of localized surface plasmons,[13–15] antireflection coating with nano-structures,[16–20] and so on. There also have been works where photovoltaic active layers were made with certain specific shapes to improve light coupling and retention. Yao et al.[21] utilized whispering gallery resonant modes induced in spherical silicon nano-shells. Mariano et al.[22] obtained a similar effect by wrapping organic solar cells around a fiber array. In our previous reports, we also introduced new solar cell structures based on shell-shaped organic active layers.[23,24] These shell-shaped structures were proposed with the aim of keeping the fabrication processes as simple as possible. In addition, because the proposed structures are made of continuous layers, they can be more robust than the ones that utilize localized components. In those previous studies, we examined cylindrical shells with a cross-section of a semicircle[23] or that of a triangle[24] via numerical analysis. It was learned that compared to the regular flat structures, the proposed cylindrical-shell-shaped structures could result in enhanced light absorption and broadened angular coverage, mainly due to light coupling to guided modes within the active layer, producing the effect of light retention.

In this work, a new shape, i.e., a hemispherical shell, is examined for the active layers (Fig. 1). The previous work[23] proved that a circular shape in two dimension (2D) brings in advantages in absorption and in angular coverage, compared to a rectangular (flat) shape. This semicylindrical shape (in yz plane), however, still appears as a rectangular shape in xz plane. It is hypothesized naturally that completing the circular shape in all directions, i.e., making it a hemispherical shape would be more advantageous in terms of absorption performances. In addition, it is well established that spherical resonators have much higher Q-factors than cylindrical ones, implying that guided modes are more strongly retained in the former.[25] This study will examine the hypothesis and show that the proposed hemispherical-shell-shaped structure has improved absorption performance and higher angular coverage than the previously reported semicylindrical-shell-shaped structure as well as than the ordinary flat structure. In this study, it was considered that the array of hemispheres is arranged with hexagonal periodicity (a unit cell is shown in Fig. 1, bottom left). The radius of the hemisphere, R (see Fig. 1) was used as the main design parameter.

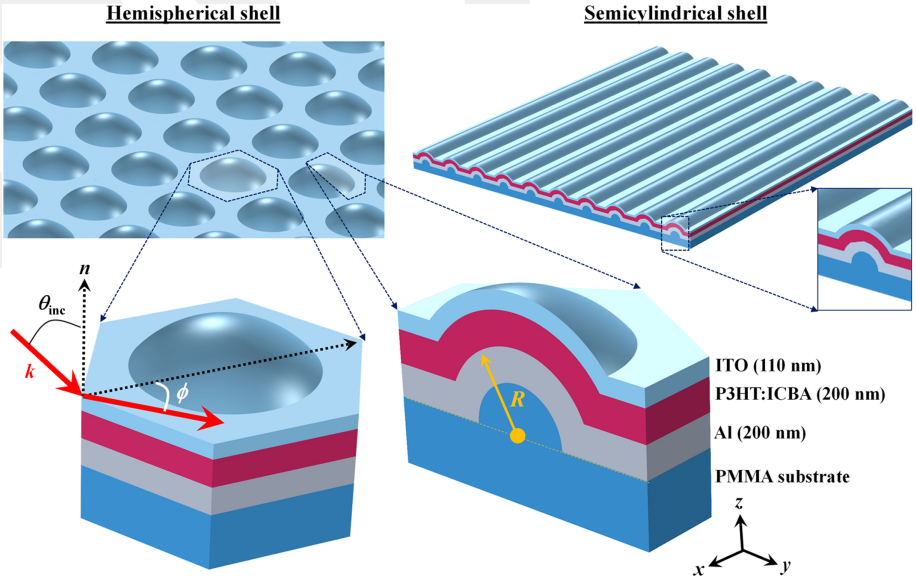

Fig. 1 Proposed photovoltaic cell structure. (Top left) bird's-eye view of a solar cell array with hemispherical-shell-shaped (HS) active layers. (Top right) Previously reported solar cell array with semicylindrical-shell-shaped (SC) active layers.[23] (Bottom left) A unit cell of an HS device. θ_{inc}: incidence angle. ϕ: azimuth angle. (Bottom right) An HS device showing its cross-section view.

The paper has the following structure. The device structures and the analytical methods will be explained in Sec. 2. Then, the results will be presented in Sec. 3. Finally, the conclusion will be provided in Sec. 4.

2 Device Structures and Analytical Methods

The layer composition of the proposed photovoltaic cells, as illustrated in Fig. 1, is aluminum (200 nm) as the bottom electrode, Poly(3-hexylthiophene-2,5-diyl) blended with indene-C60 bisadduct (P3HT:ICBA, 200 nm) as the active layer, and indium tin oxide (ITO, 110 nm) as the transparent top electrode. For the device operation, buffer layers must be included as well. However, they are not considered in the analysis for their thinness. It is noteworthy that the proposed structure is applicable to other organic active materials as well. Those aforementioned layers are to be conformally coated on the hemispherically shaped polymer substrate. To maintain the shape of the polymer substrate's front surface in the polymer active layer, soft lithography technologies, such as microcontact printing,[26] can be utilized to transfer the polymer active layer from a temporary substrate to the final substrate. Other thin film layers can be deposited using conventional deposition methods, such as sputtering.

Flexible polymers, such as polymethyl methacrylate (PMMA), PI (polyimide), etc., can be used as the substrate, which can be made to have the extruding array of hemispheres at the front surface via one of the following methods (Fig. 2): (I) thermal reflow of resist,[27,28] (II) grayscale lithography,[29,30] or (III) nanosphere lithography (NSL) followed by two steps of casting and reactive ion etching (RIE).[31] The method (I) utilizes thermal reflow, i.e., morphological change of a material when heated over the glass transition temperature, driven by surface tension.

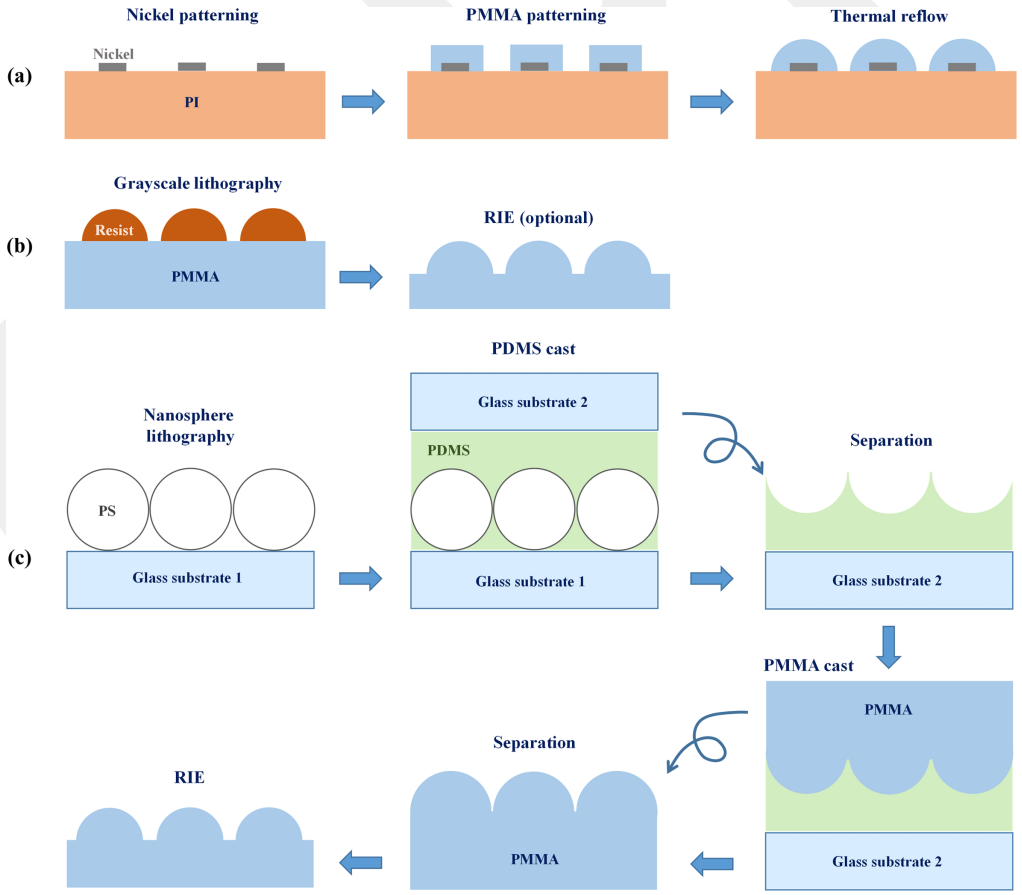

Fig. 2 Fabrication methods of a PMMA or a PMMA/PI substrate with hemispherical shapes protruding from a front surface. (a) Thermal reflow. (b) Grayscale lithography + (optional) RIE. (c) NSL + two steps of casting + RIE, adopted from Ref. 31. In method (III), the third temporary glass substrate for PMMA casting is omitted from the illustration for simplicity. PS: polystyrene.

Thermal reflow can turn a cylindrical shape into a part of a sphere. One of the key points in utilizing this method for the proposed structure is to control the contact angle of the spherical shape. Reference 28 presents a fabrication process where inclusion of nickel pillars makes it possible to obtain a contact angle over 90 deg (up to 132 deg) from reflowed PMMA. The method (I) starts with the patterning of nickel on a PI substrate. PI is selected as the substrate material for its higher glass transition temperature (250°C to 340°C) than that of PMMA (90°C to 110°C) so that the substrate is not affected much during the thermal reflow of PMMA. The next step is to pattern PMMA cylinders by lithography [deep ultraviolet (UV), e-beam, or X-ray] or by RIE with regular UV resist as an etching mask. Then, thermal reflow is followed. The contact angle of the PMMA can be controlled by reflow temperature, reflow time, and dimensions of the nickel pillars.

The method (II) relies on grayscale lithography. In grayscale lithography, spatial variation in the dose amount can produce controlled three-dimensional (3D) shapes after development. Depending on the material of the resist used in the lithography and the achievable shape with the lithography, the patterned resist can be used as it is as a part of the substrate or as an etching mask for the follow-up RIE process. If an RIE process is included, the process is stopped after all the resist masks are consumed. Efforts are needed to find an optimal etch rate ratio between the resist and PMMA so that a proper shape of a hemisphere is formed in the substrate. Should a rough surface result after the RIE process, it can be smoothed by a moderate thermal reflow process.

The method (III) is the most complicated one among the three proposed methods. It is based on NSL and casting.[31] In NSL, colloidal suspension of beads (such as PS) is dropped on a temporary glass substrate. After evaporation of water, a hexagonal array of PS remains on the substrate. Next, a mixture of polydimethylsiloxane (PDMS) and curing agent is cast on the PS array, and the second temporary glass is placed on PDMS. After curing, the PDMS stamp is detached from the PS/glass substrate. Then, the second casting, this time with PMMA, is performed on the PDMS stamp. Anti-adhesion agent can be applied between PMMA and PDMS for easier separation. Finally, an RIE process can be performed on the PMMA substrate to obtain the optimum geometries.

For the optical analysis of the proposed structures, 3D finite element analysis (FEA) was carried out by using COMSOL Multiphysics® (version 5.2). As the light source, either transverse electric (TE)- or transverse magnetic (TM)-polarized plane wave was launched from the air. The refractive indices and extinction coefficients of P3HT:ICBA were obtained from Ref. 22. The analysis was conducted with one unit cell (Fig. 1, bottom-left). While Floquet–Bloch periodic boundary conditions were applied on the parallel side surfaces, pair by pair, a perfectly matched layer was set up at the bottom surface of the substrate. Absorption spectra, $\alpha(\lambda, \theta_{\text{inc}}, \phi)$, in the active layer were obtained via FEA, and from this, the integrated absorption, $\text{IA}(\theta_{\text{inc}}, \phi)$ was calculated using the following equation:

$$\text{IA}(\theta_{\text{inc}}, \phi) = \frac{\int_{\lambda_1}^{\lambda_2} \alpha(\lambda, \theta_{\text{inc}}, \phi) I_{\text{AM1.5G}}(\lambda) \text{d}\lambda}{\int_{\lambda_1}^{\lambda_2} I_{\text{AM1.5G}}(\lambda) \text{d}\lambda}, \tag{1}$$

where $I_{\text{AM1.5G}}(\lambda)$ is the standard AM1.5G spectral irradiance of the Sun. λ_1 and λ_2 were 300 and 750 nm, respectively, determined by the range of the optical properties of P3HT:ICBA available in the literature.[22] IA is a function of both incidence angle (θ_{inc}) and azimuth angle (ϕ). However, as will be shown later, IA is much more heavily influenced by θ_{inc} than it is by ϕ. From $\text{IA}(\theta_{\text{inc}})$, IA_{ave}, the average integrated absorption over a range (0 deg to 89 deg) of incidence angles, was calculated as an indication of the absorption capability for possible incidence angles. Another figure of merit, EF_{ave}, the average enhancement factor, was calculated as a ratio of IA_{ave} between the proposed device and a flat device. The third figure of merit, θ_{cov}, a measure of an angular coverage (omnidirectionality), was defined differently from the previous report[24] as the incidence angle where IA becomes 90% of $\text{IA}_{\text{ave,0–45}}$. $\text{IA}_{\text{ave,0–45}}$ is defined as the average value of IA between 0 deg and 45 deg of incidence angles where the IA curves are relatively flat. For the case of hemispherical-shell-shape, $R = 1$ μm, and TE polarization as an example (see Fig. 6), $\text{IA}_{\text{ave,0–45}}$ is found as 81.9%, and IA becomes 90% of that value at around 82 deg, which becomes θ_{cov} for this case.

The simulation study was carried out with the sole PMMA substrate, i.e., based on the fabrication methods (II) and (III). It should be noted that, however, the results with the PMMA/PI substrate embedded with nickel pillars (method I) are not expected to be different from those results because light penetration through the bottom electrode layer is extremely low.

3 Results

Figure 3 presents examples of spatial distributions of electric fields for the proposed structure, sliced at multiple locations along the x direction. The figure also includes electric field distributions of the SC device and the ordinary flat device for comparison. Figures 3(a)–3(d) show that light is guided through the active layer of the HS device, even at a very high incidence angle (e.g., 80 deg). The SC device also induces light guiding as can be seen from Figs. 3(e)–3(h). However, the light guiding in the SC device is not as strong as that in the HS device at high incidence angles. It can be clearly observed [Fig. 3(f)] that with TE polarized input at 80° of incidence, only very weak guiding (understood from the saturated field intensity in the air) is present in the active layer. For the TM polarization [Figs. 3(g) and 3(h)], a substantial portion of light is observed leaving from the ITO surface, which does not occur as strongly in the case of the HS device. For the flat structure [Fig. 3(i)], no light guiding is observed as expected.

This effect of light guiding is reflected in absorption spectra, $\alpha(\lambda)$ (Fig. 4). For a flat structure, the absorption is significantly reduced at 80 deg of incidence for TE polarization compared to those at 60 deg and 0 deg (more moderate reduction is observed for TM polarization). It is, however, only slightly weakened in the case of the hemispherical-shell-shaped device at 80 deg of incidence. This is not the case for the semicylindrical devices, which show clear weakening of absorption at 80 deg for both polarizations. Therefore, it can be concluded that the HS device has

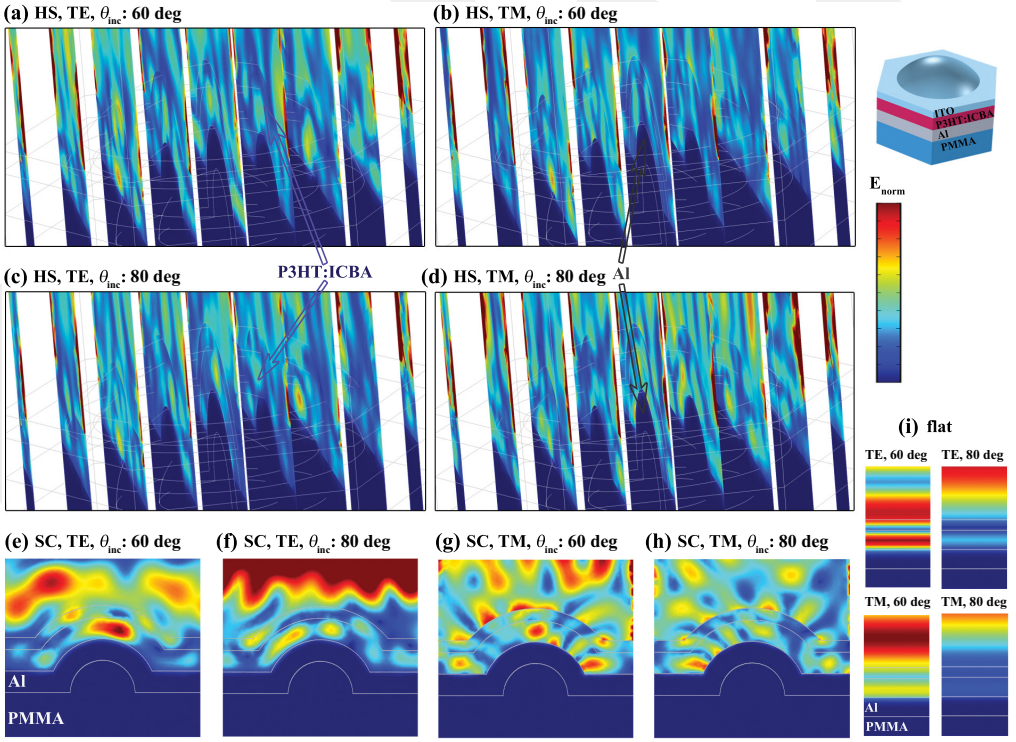

Fig. 3 Calculated electric field norms in (a)–(d) hemispherical-shell-shaped (HS), (e)–(h) semicylindrical-shell-shaped (SC), and (i) ordinary flat structures at two different incidence angles (60 deg and 80 deg) and with two different (TE and TM) input polarizations. Wavelength (λ): 650 nm. R: 0.5 μm for HS and SC structures. ϕ: 0 deg for HS structure. Color map indicates field strength (red: highest, blue: lowest). Gray lines indicate layer boundaries. (a)–(h) For clearer visualization, fields are normalized according to the highest field strength within the active layer for each plot. (i) Fields are normalized with respect to the highest field strength within the simulation domain.

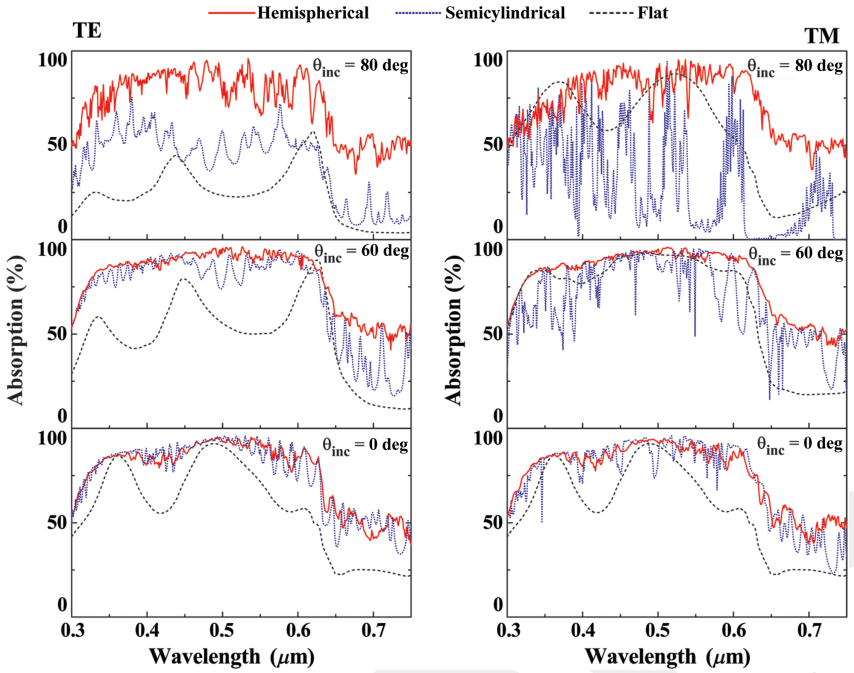

Fig. 4 Absorption spectra $\alpha(\lambda)$ in hemispherical- (red, solid) and semicylindrical-shell-shaped (blue, dotted) active layers at three different incidence angles (θ_{inc}: 0 deg, 60 deg, and 80 deg). R: 0.5 μm. For HS, $\phi = 0$ deg. $\alpha(\lambda)$ for a flat structure (black, dashed) is included in the graphs as a reference.

clear advantages at high incidence angles over the SC devices. At the incidence angles of 0 deg and 60 deg, the absorption spectra are relatively close to each other between two types (HS and SC) of devices. In the case of the HS device, the absorption spectra are higher than those of the flat structure at all incidence angles. In the case of the SC device, however, the absorption spectra of TM polarization are lower than those of the flat structure at 80 deg of incidence.

Effects of azimuth angle on absorption were studied and presented in Fig. 5. At low incidence angles, the effect of azimuth angle on the absorption was negligible. As the incidence angle increases, the effect of azimuth angle begins to appear, starting from longer wavelengths. At 30 deg of incidence, dependence of absorption on ϕ is clearly seen at 700 nm for both polarizations whereas curves are quite flat at shorter (320 and 500 nm) wavelengths. This is because the geometrical effect is more pronounced at longer wavelengths. At 60 deg of incidence, fluctuation in absorption starts to be observed at 500 nm as well, while it becomes stronger at 700 nm. At 85 deg of incidence, absorption variation becomes quite substantial, except for the case of 320 nm with TE polarization. It is interesting to observe that the absorption variation is remarkable at 320 nm for TM polarization. The reason for high ϕ-dependent absorption variation at a high incidence angle can be understood from the fact that the periodicity of the array lies on the xy plane. Light with a high incidence angle enters the structure more parallel to this xy plane so that it is more heavily affected by the periodicity, in other words, by the angle the Poynting vector makes with the unit vectors of the array. When light enters the structure close to the normal (i.e., perpendicular to xy plane), it sees the periodicity less. It will be shown later (Fig. 7) that the overall effect of azimuth angle on the integrated absorption is not significant nevertheless.

Comparison of integrated absorption, IA(θ_{inc}), among different structures (HS, SC, and flat) is presented in Fig. 6. It clearly shows that the HS devices result in stronger absorption than the SC devices when compared at the same R values. The differences stand out more at high θ_{inc} as learned from Fig. 4. With TE polarization, both types (HS and SC) of devices demonstrate much stronger absorption than a flat structure. In the case of TM polarization, compared to a flat device, the SC devices exhibit higher absorption at low θ_{inc} but lower absorption at high θ_{inc}. On the other hand, the HS devices show higher absorption than a flat device for all incidence angles. This is one of the strong points of the HS devices. The graphs at the bottom of Fig. 6 present the IA only for the HS devices at different R values. Improvements in absorption are clearly

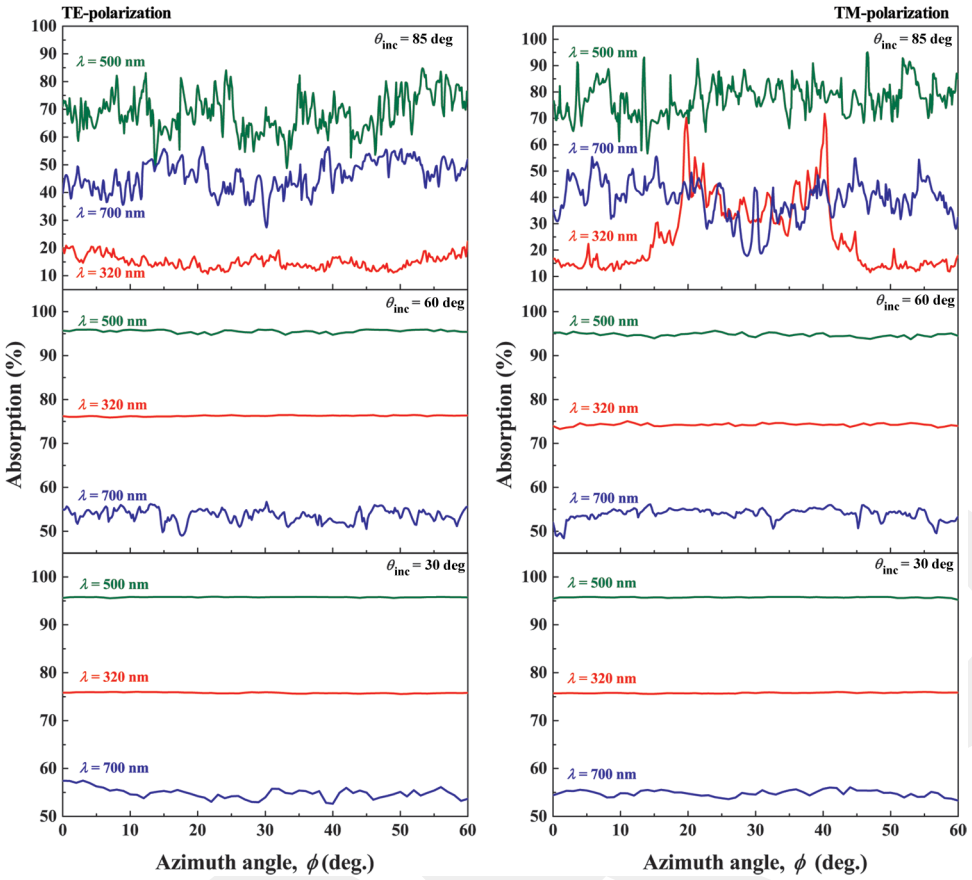

Fig. 5 Absorption (α) in hemispherical-shell-shaped active layers as a function of azimuth angle (ϕ) at three different wavelengths (λ: 320, 500, and 700 nm) and at three different incidence angles (θ_{inc}: 30 deg, 60 deg, and 85 deg). R: 1 μm.

noticeable as R increases from 0.5 to 1 μm. However, IA curves look almost the same between $R = 1$ μm and $R = 1.5$ μm. Therefore, it can be concluded that 1 μm of R is sufficient for the HS device to benefit from the structure. This is a favorable conclusion because it is relatively easier to realize the proposed structure for a smaller value of R in practice.

Table 1 summarizes absorption performances and angular coverage of both types (HS and SC) of devices. The absorption performance indicators (IA_{ave} and EF_{ave}) of the HS devices are substantially higher than those of the SC devices at all R values. The disparity between the two devices, however, becomes narrower as R increases. As R increases from 0.5 to 1.5 μm, EF_{ave} increases just by 4.4% (TE) and 3.8% (TM) in the HS devices, whereas it does so by 8.6% (TE) and 10.2% (TM) in the SC devices. This is because the absorption performances of the HS devices are not heavily affected by the R values, while the SC devices are more dependent on the R values. Nevertheless, the HS devices exhibit clear advantages over the SC devices at high incidence angles, which is beneficial in terms of the angular coverage. At all values of R, the angular coverage θ_{cov} was significantly higher in the HS devices (between 77 deg and 82 deg) than in the SC devices (between 62 deg and 76 deg). Compared to TE polarization, TM polarization results in smaller values of EF_{ave} due to the fact that in a flat structure, which is used as the reference, absorption is higher with TM polarization than with TE polarization owing to reduced TM wave reflection around the Brewster angle. For the HS devices, the highest EF_{ave} values were found to be 1.66 (TE) and 1.36 (TM), and the widest θ_{cov} were 81 deg for TE- and 82 deg for TM-polarization.

It is meaningful to compare the active layer volumes between the two types of devices because a larger volume can be thought to be advantageous in terms of absorption. For the same footprint and the active layer thickness, the volume ratio of HS over SC is 1.093 when $R = 1.5$ μm, which decreases to 1.063 for R of 1 μm and to 0.988 for R of 0.5 μm. This trend

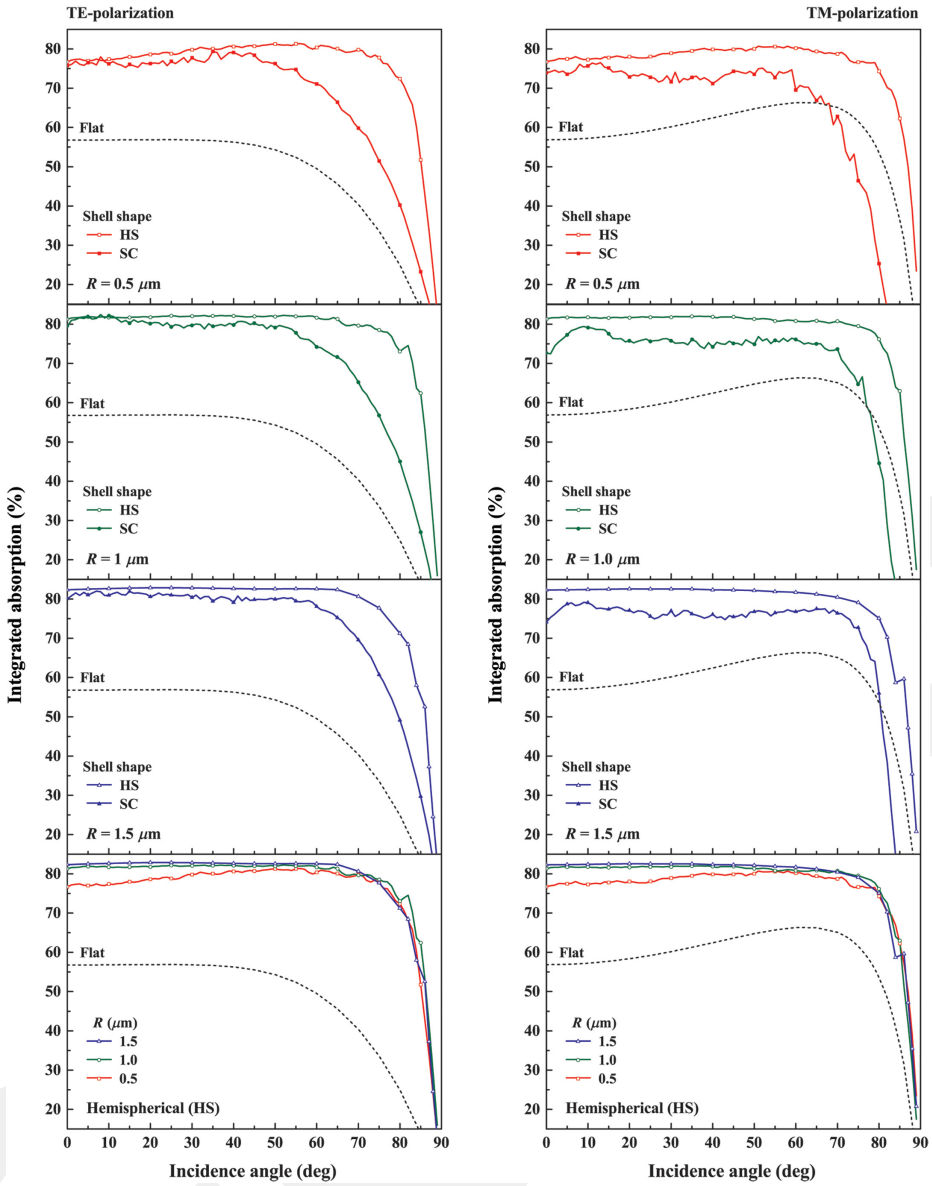

Fig. 6 Integrated absorption, $IA(\theta_{inc})$ in hemispherical- (HS, open symbols) and semicylindrical-shell-shaped (SC, closed symbols) active layers for various R values. Dashed curves are for a flat structure device. For HS, $\phi = 0$ deg.

Table 1 Absorption performances, enhancement factors, and angular coverage. For HS, $\phi = 0$ deg.

R (μm)		0.5		1		1.5		Flat	
polarization		TE	TM	TE	TM	TE	TM	TE	TM
IA_{ave}(%)	HS[a]	75.9	76.5	78.5	78.4	79.4	79.7	47.7	58.6
	SC[b]	66.9	63.2	70.7	68.2	72.3	69.8		
EF_{ave}	HS	1.59	1.31	1.65	1.34	1.66	1.36		
	SC	1.40	1.08	1.48	1.16	1.52	1.19		
θ_{cov}(°)	HS	81	82	81	81	77	81		
	SC	62	67	63	73	67	76		

[a]Hemispherical-shell-shaped device
[b]Semicylindrical-shell-shaped device

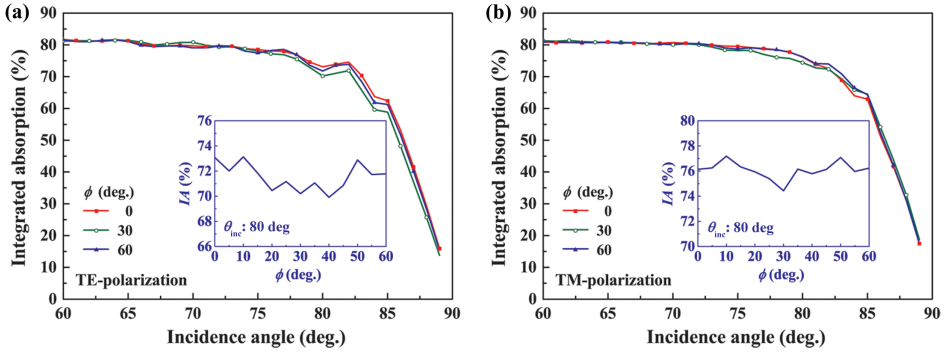

Fig. 7 Integrated absorption, IA(θ_{inc}) in hemispherical-shell-shaped active layers for various azimuth angles, ϕ. (a) TE-polarization and (b) TM-polarization. $R = 1$ μm. (Insets) IA(ϕ) when $\theta_{inc} = 80$ deg.

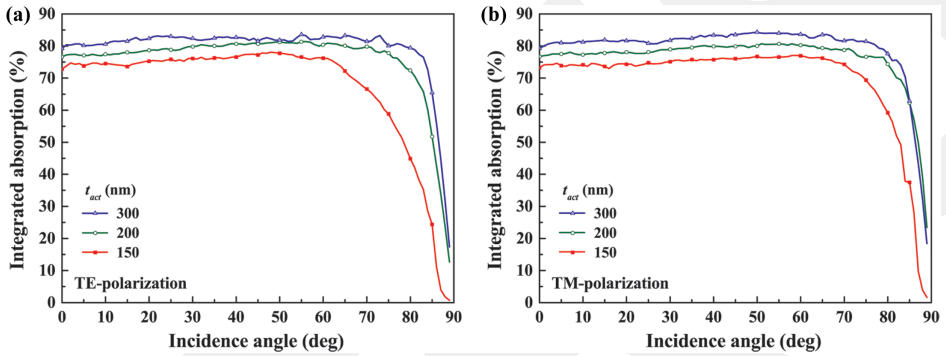

Fig. 8 Integrated absorption, IA(θ_{inc}) in hemispherical-shell-shaped active layers for various active layer thicknesses, t_{act}. (a) TE-polarization and (b) TM-polarization. $R = 0.5$ μm, and $\phi = 0$ deg.

is found to be the opposite in EF_{ave} ratio, which increases as R decreases. For TE-polarization, the EF_{ave} ratio of HS over SC increases from 1.092 at $R = 1.5$ μm to 1.136 at $R = 0.5$ μm. Therefore, it can be understood that the difference in the active layer volume between the two types of shells does not play a significant role in the absorption enhancement.

Figure 7 presents the effect of azimuth angle on the integrated absorption. As can be seen from the figure, the azimuth angle does not have significant effects on the integrated absorption. Slight differences are observed only at high incidence angles (>70 deg) for both polarizations as expected from the results presented in Fig. 5. For a given azimuth angle, absorption increases at some wavelengths while it decreases at other wavelengths, when compared to the magnitude of absorption at $\phi = 0$ deg. Due to this averaging effect, the dependence on ϕ becomes unsubstantial overall. Insets in Fig. 7 also show that the integrated absorption is not much affected by azimuth angle. Figure 8 presents the effect of the active layer thickness, t_{act} to the integrated absorption of hemispherical-shell-shaped devices. As expected, IA increases according to the active layer thickness.

4 Conclusion

FEA study was conducted to examine a proposed structure of hemispherical-shell-shaped active layers with a focus on absorption and omnidirectionality characteristics. Absorption enhancement of the proposed structure was up to 66% and 36% for TE- and TM-polarization, respectively, when compared to a flat-structure device. It was also found that the absorption enhancement and the angular coverage of the hemispherical-shell devices are higher than those of the previously reported semicylindrical-shell devices, which confirms the hypothesis set up in Sec. 1. For R of 0.5 μm, the HS device showed 13% (TE) and 21% (TM) higher IA_{ave} than

the SC device. The HS devices outperform the SC devices, especially at high incidence angles. Decent absorption was maintained up to 81 deg (TE) and 82 deg (TM) of incidence angle in the HS devices. By comparison, the angular coverage was below 76 deg in the SC devices. The improvements in absorption and angular coverage are attributed to enhanced light guiding in the active layer. It was concluded that 1 μm of R value is sufficient to take benefits from the HS structure. It was also concluded that the active layer volume differences between the HS and the SC shells do not play a significant role in the absorption enhancement. In terms of the azimuth angle, it was found that it has a non-negligible effect to absorption characteristics in the HS devices. However, its overall effect to the integrated absorption turned out to be insignificant after taking averages.

It is envisaged that with the improved absorption and omnidirectionality characteristics, the proposed hemispherical-shell-shaped active layers will be found beneficial in various application areas of the organic solar cells (OSCs), such as biomedical devices,[32] semitransparent OSC applications, including power generation windows and greenhouses,[33,34] indoor applications, including internet-of-things (IOTs),[35] and so on.

Disclosures

The author declares no conflicts of interest.

Code and Data Availability

All data in support of the findings of this paper are available within the article.

Acknowledgments

This work was partially supported by the research fund of Abdullah Gül University (Grant No. FOA-2016-49).

References

1. M. Niggemann et al., "Light trapping in organic solar cells," *Phys. Status Solidi-a* **205**, 2862–2874 (2008).
2. O. A. Abdulrazzaq et al., "Organic solar cells: a review of materials, limitations, and possibilities for improvement," *Part. Sci. Technol.* **31**, 427–442 (2013).
3. T. Ameri et al., "Organic ternary solar cells: a review," *Adv. Mater.* **25**, 4245–4266 (2013).
4. N. Yeh and P. Yeh, "Organic solar cells: their developments and potentials," *Renew. Sustain. Energy Rev.* **21**, 421–431 (2013).
5. Z. Tang, W. Tress, and O. Inganas, "Light trapping in thin film organic solar cells," *Mater. Today* **17**, 389–396 (2014).
6. C. Yan et al., "Non-fullerene acceptors for organic solar cells," *Nat. Rev. Mater.* **3**, 18003 (2018).
7. O. O. Amusan et al., "Different interface engineering in organic solar cells: a review," *Chem. Methodol.* **3**, 425–441 (2019).
8. K. Sreejith et al., "A comprehensive investigation of the potential of metal assisted chemical etched (mace) nano-textures over conventional micron-sized iso-textures for industrial silicon solar cell applications," *Sol. Energy* **230**, 874–882 (2021).
9. T. M. Mercier et al., "High symmetry nano-photonic quasi-crystals providing novel light management in silicon solar cells," *Nano Energy* **84**, 105874 (2021).
10. A. Ali et al., "Improving the efficiency of the organic solar cell (CuPc/c60) via pedot: PSS as a photoconductor layer doped by silver nanoparticles," *Results Phys.* **16**, 102819 (2020).
11. Z. Kordrostami and A. Yadollahi, "High absorption enhancement of invert funnel and conical nanowire solar cells with forward scattering," *Opt. Commun.* **459**, 125059 (2020).
12. Sachchidanand and D. Samajdar, "Light-trapping strategy for PEDOT:PSS/C-Si nanopyramid based hybrid solar cells embedded with metallic nanoparticles," *Sol. Energy* **190**, 278–285 (2019).
13. X. Liu et al., "Broadband and wide-angle light absorption of organic solar cells based on multiple-depths metal grating," *Opt. Express* **27**, A596–A610 (2019).
14. G. T. Mola et al., "Local surface plasmon resonance assisted energy harvesting in thin film organic solar cells," *J. Alloys Compd.* **856**, 158172 (2021).
15. B. Wei et al., "Recent progress of surface plasmon-enhanced light trapping in GaAs thin-film solar cells," *Plasmonics* **18**, 2009–2029 (2023).

16. J. Grandidier et al., "Light absorption enhancement in thin-film solar cells using whispering gallery modes in dielectric nanospheres," *Adv. Mater.* **23**, 1272–1276 (2011).
17. A. P. Amalathas and M. M. Alkaisi, "Efficient light trapping nanopyramid structures for solar cells patterned using UV nanoimprint lithography," *Mater. Sci. Semicond. Process.* **57**, 54–58 (2017).
18. T. K. Das, P. Ilaiyaraja, and C. Sudakar, "Whispering gallery mode assisted enhancement in the power conversion efficiency of DSSC and QDSSC devices using TiO_2 microsphere photoanodes," *Appl. Energy Mater.* **1**, 765–774 (2018).
19. F. F. Mahani and A. Mokhtari, "TiO_2 circular nano-gratings as anti-reflective coatings and potential color filters for efficient organic solar cells," *J. Nanoelectron. Optoelectron.* **13**, 1624–1629 (2018).
20. A. Jangjoy, H. Bahador, and H. Heidarzadeh, "A comparative study of a novel anti-reflective layer to improve the performance of a thin-film GaAs solar cell by embedding plasmonic nanoparticles," *Plasmonics* **16**, 395–401 (2021).
21. Y. Yao et al., "Broadband light management using low-q whispering gallery modes in spherical nanoshells," *Nat. Commun.* **3**, 664 (2012).
22. M. Mariano et al., "Light coupling into the whisphering gallery modes of a fiber array thin film solar cell for fixed partial sun tracking," *Sci. Rep.* **4**, 4959 (2014).
23. D. Hah, "Absorption enhancement by semi-cylindrical-shell-shaped structures for an organic solar cell application," *Appl. Opt.* **59**, 8645–8652 (2020).
24. D. Hah, "Shell-shaped active layers for omnidirectional organic photovoltaic cells," *J. Photonics Energy* **12**, 048501 (2022).
25. J. Krupka et al., "Extremely high-q factor dielectric resonators for millimeter-wave applications," *IEEE Trans. Microw. Theory Tech.* **53**, 702–712 (2005).
26. K. Choonee and R. R. A. Syms, "Multilevel self-aligned microcontact printing system," *Langmuir* **26**, 16163–16170 (2010).
27. C. Dai, K. Agarwal, and J.-H. Cho, "Ion-induced localized nanoscale polymer reflow for three-dimensional self-assembly," *ACS Nano* **12**, 10251–10261 (2018).
28. X. Liang et al., "The fabrication of microlens array in PMMA material with the assistant of nickel pillars by LIGA technology and thermal reflow method," *Microsyst. Technol.* **29**, 763–771 (2023).
29. J. Loomis et al., "Grayscale lithography—automated mask generation for complex three-dimensional topography," *J. Micro/Nanolithogr. MEMS MOEMS* **15**, 013511 (2016).
30. X. Tong et al., "A study of greyscale electron beam lithography for a 3D round shape kinoform lens for hard x-ray optics," *Microelectron. Eng.* **234**, 111435 (2020).
31. M. R. Goncalves et al., "Plasmonic nanostructures fabricated using nanosphere-lithography, soft-lithography and plasma etching," *Beilstein J. Nanotechnol.* **2**, 448–458 (2011).
32. N. Cui et al., "Stretchable transparent electrodes for conformable wearable organic photovoltaic devices," *NPJ Flexible Electron.* **5**, 31 (2021).
33. H. Yu et al., "Semi-transparent organic photovoltaics," *Chem. Soc. Rev.* **52**, 4132–4148 (2023).
34. W. He et al., "In situ self-assembly of trichlorobenzoic acid enabling organic photovoltaics with approaching 19% efficiency," *Adv. Funct. Mater.* 2313594 (2023).
35. M. Jahandar, S. Kim, and D. C. Lim, "Indoor organic photovoltaics for self-sustaining IoT devices: progress, challenges and practicalization," *ChemSusChem* **14**, 3449–3474 (2021).

Dooyoung Hah is an assistant professor at Abdullah Gül University. He received his PhD in electrical engineering from KAIST in 2000. He also worked at Louisiana State University, University of California Los Angeles, and Electronics and Telecommunications Research Institute. He has authored and co-authored more than 90 papers in journals and conference proceedings. He also holds 11 patents. He served as a program chair for EKC (Europe-Korea Conference on Science and Technology) 2022. He also has been serving as a technical committee member for the Symposium on Design, Test, Integration and Packaging of MEMS and MOEMS (DTIP) since 2018. His current research interests include nano-/micro-systems, sensors, energy harvesting devices, photovoltaic devices, wearable electronics, and integrated photonics.